

# Finite element analysis of floatation of rectangular tunnels following earthquake induced liquefaction

SSC Madabhushi\* and SPG Madabhushi\*\*

\*PhD student, Department of Engineering, University of Cambridge, Cambridge, UK

\*\* Professor of Civil Engineering, University of Cambridge, Cambridge, UK

## Abstract

Underground structures such as tunnels, pipelines, car parks etc. can suffer severe damage during strong earthquake events. As many of these structures are buoyant, soil liquefaction due to earthquake loading can result in their floatation. In this paper, the floatation of rectangular tunnels, normally constructed by the cut-and-cover method, is investigated using dynamic finite element analyses. Sinusoidal and more realistic earthquake input motions are considered. The acceleration response of the tunnel and the soil surface following soil liquefaction is investigated. The generation of excess pore pressures in the soil around the tunnel and the consequent floatation of the tunnel are observed for both types of input motions. It will be shown that the amount of tunnel uplift depends on the type of input motion with the sinusoidal motion leading to a significantly larger uplift compared with the more realistic Kobe motion. Further, the effect of soil permeability on the floatation of the rectangular tunnel is investigated. It will be shown that tunnels can suffer floatation in finer soils with low permeabilities, whilst coarser soils with high permeability can lead to tunnel settlements owing to the rapid re-consolidation of the liquefied soils. The average axial strains in the soil above the tunnel will be shown to decrease with decreasing permeability.

**Keywords:** earthquakes, liquefaction, settlement, tunnel, uplift

## Introduction

With the increase in demand on land in urban areas, there is a growing need to locate vital lifelines below ground. However, underground structures such as transportation tunnels and utility pipelines are susceptible to damage during a major earthquake. Seismic behavior of tunnels and other underground structures can be studied using numerical analyses or physical testing. Cilingir and Madabhushi [1,2,3] investigated the seismic response of square tunnels using both dynamic centrifuge testing and finite element analyses for tunnels of different flexibility ratios subjected to a variety of ground motions. Seismic behaviour of tunnels is even more important when the ground surrounding these structures is susceptible to liquefaction. Metro tunnels, large underground car parks, pipelines and manholes can suffer significant uplift in liquefied soil as observed in numerous earthquake events including the 2011 Great East Japan Earthquake [4]. An example of the floatation of a pipeline during this earthquake is shown in Fig. 1. In this figure it can be seen that the pipeline floatation caused the

ground surface to heave. The underground structures are generally subjected to a buoyant force due to their lower submerged unit weight compared to the surrounding soil. Under static conditions, the weight and shear strength of the overlying soil inhibits the floatation. In the event of liquefaction, the soil loses most of its shear strength and the structure may float as a result. Existing major lifelines built in earthquake-prone areas include the George Massey highway tunnel in Vancouver (Canada), San Francisco's Bay Area Rapid Transit (BART) tunnel, Claremont water tunnels (USA) and large diameter natural gas pipelines in New Mexico, Japan and Canada. Other seismically active regions are also planning or are in the midst of constructing massive lengths of submersible tunnels in liquefiable soils such as the Thessaloniki Highway Tunnel and Marmaray Rail Tunnel in Greece and Turkey respectively. Several cities in India are also in the midst of planning and constructing large metro tunnels, sometimes sections of which go below the existing water table. Such tunnels can carry thousands of commuters during peak hours and evidently pose extreme concerns to public safety in the event of a strong earthquake. Even a small amount of uplift of tunnel segments following soil liquefaction can break longitudinal joints and lead to flooding.

The possibility of uplift of underground structures in a major earthquake was supported by several numerical and experimental analyses. Numerical analyses carried out by Yang *et al.* [5] on the George Massey Tunnel and Sun *et al.* [6] on the BART tunnel showed significant floatation. However, these analyses were carried out for very specific cases and site conditions. However, the basic failure mechanisms were substantiated with findings from centrifuge experiments carried out by Adalier *et al.* [7] and Chou *et al.* [8] who observed a significant amount of sand displacing towards the tunnel invert when simulating conditions of the George Massey Tunnel and BART tunnel respectively. The uplift was observed to be affected by both the input earthquake shaking intensity and the generation of excess pore pressure. Sasaki *et al.* [9] also noted that the uplift displacement of pipes was significant when input acceleration was large or when the density of sand was low in their centrifuge tests. In the case of manholes, Tobita *et al.* [10] postulated that the primary cause of uplift is the reduction of the effective confining stress near the bottom of a manhole due to strong shaking.

At present, geotechnical studies carried out on the floatation of underground structures in liquefiable soil are limited as pointed out by Ling *et al.* [11]. The factor of safety against floatation adapted from Koseki *et al.* [12] was developed further and verified with centrifuge experiments for pipes [11] and manholes [10]. However, such factor of safety procedures only provide the triggering condition of uplift and fall short of predicting the final uplift displacement of underground structures [10]. Dynamic centrifuge tests were also carried out by Chian and Madabhushi [13, 14], Chian *et al.* [15] to investigate the post-liquefaction floatation of circular tunnels. Numerical analysis was successfully conducted to simulate the dynamic response of the soil and pipe up to the stage of initial liquefaction

[16]. However, large soil strain simulation during the post-liquefaction phase remains a challenge to date with conventional numerical methods.

The soil deformation around the uplifted structure was also investigated from field observations in order to provide a more holistic understanding of the uplift mechanism of buoyant underground structures. Further analysis on the performance of underground sewer pipes in Urayasu City, Chiba Prefecture near Tokyo subjected to the ground motion following the 2011 Great Hanshin Japan Earthquake showed significant uplift displacement in liquefiable soil deposit which is in agreement with the damage of these pipelines observed [17].

Much of the research on floatation of tunnels or pipelines outlined above falls into two categories that either investigated circular tunnels or studied specific tunnel configurations such as George Massey tunnel in Vancouver. In this paper the main focus will be on floatation of rectangular tunnels that are located in liquefiable soils. This type of rectangular tunnels are normally constructed for metro lines such as the ones in Delhi or Kolkata using cut-and-cover method of construction, especially when the embedment depth of the tunnel is relatively shallow. It is therefore important to understand both the seismic behaviour of such tunnels and the uplift suffered by the tunnel sections under different earthquake motions and in soils of different permeabilities.

## Finite element formulation

The finite element method is a well-established technique that is used to solve problems in geotechnical earthquake engineering. For solving the problem of tunnel floatation, the effective stress based FE code SWANDYNE was used [18]. This is a fully coupled code that uses solid phase displacement and fluid phase pore pressure ( $u-p$ ) formulation and solves the Biot's equations for a two-phase medium. This formulation is described in detail by Madabhushi and Zeng [19] and therefore not repeated here for brevity. The FE analyses were carried under plane strain assumptions as a long, rectangular tunnel is being modelled. The FE discretization was carried out to match the boundary value problem dimensions as shown in Figs. 2. As shown in this figure the dimensions of the domain are taken as 35 m  $\times$  19 m. The rectangular tunnel had the dimensions of 10 m  $\times$  4 m to represent a metro tunnel that can accommodate up and down railway lines. The embedment depth of the tunnel was 10 m below ground surface giving an embedment ratio of 1. The static factor of safety against floatation of such a tunnel is about 1.6. The discretization was carried out in two distinct zones i.e. the loose sand and the tunnel cross-section as shown in Fig. 2. The boundary conditions used for all the analyses described in this paper are shown in Fig. 3. The base nodes of the FE mesh were

assumed to be fixed in both  $x$  and  $y$  directions. The side boundary nodes were fixed in the  $x$  direction but free to move in the  $y$  direction. In addition the side boundary nodes at the same elevation were all ‘tied’ together, i.e. they experience the same accelerations and hence the same nodal forces. The earthquake loading is applied as a time-varying input acceleration to all of the base nodes.

The FE elements used for the saturated sandy soil were iso-parametric and had 12 nodes (8 solid nodes and 4 fluid nodes giving 20 degrees of freedom per each element). The tunnel section was modelled using 8 noded elements. In total there were 665 elements in the FE mesh, 7820 nodes and 13029 degrees of freedom after allowing for the restraints. The FE mesh has been designed to allow shear wave propagation before the onset of liquefaction. The minimum time step was chosen following the guidelines for liquefaction problems given by Haigh et al [20]. The finer mesh therefore satisfies the convergence criteria for the nonlinear material model used for saturated soil.

The saturated sandy soil was simulated using material models outlined below. However, the tunnel itself is modelled as a ‘stiff’ inclusion into the ground i.e. the flexibility of tunnel walls is not modelled. The saturated unit weight of the soil is taken as  $18.9 \text{ kN/m}^3$  while that of the tunnel is taken as  $5.61 \text{ kN/m}^3$ . This was calculated based on the size of the tunnel, estimated weight of the tunnel linings and the buoyancy forces acting on the tunnel. The soil properties used in all analyses are shown in Table 1. These properties are reflective of typical fine Silica sands used in laboratory experiments at the Schofield Centre such as Fraction E sand or Hostun sand.

### *Numerical Analyses*

Numerical analysis of the tunnel in a horizontal, saturated sand bed that is subjected to earthquake loading is a complex problem. The constitutive model for the soil must be able to generate positive excess pore pressures when subjected to cyclic shear stresses induced by the earthquake loading. For this purpose the P-Z Mark III model was used. However a preliminary analysis of the problem is required with the Mohr-Coulomb constitutive model to establish the static stresses in the soil elements. The water table is taken to be at the soil surface as shown in Fig. 2. The procedure adopted was to carry out a static run in which the geo-static stresses are generated and the tunnel equilibrium is established despite the tendency of the tunnel to float. This includes the establishment of effective stresses and hydrostatic pore pressures. In this run the soil elements are modelled as a Mohr-Coulomb material. In the dynamic run, the final stress state from the static run was used as the starting point with the P-Z Mark III constitutive model for the soil elements.

Another important consideration in the dynamic FE analyses is the modeling of semi-infinite extent of the soil medium. Appropriate nodes of the outer elements on the left and

right hand sides, as shown in Fig. 3, that represent the model container are tied together. This would ensure that these nodes will experience the same accelerations and nodal forces.

### ***Constitutive Models***

The constitutive model used for the tunnel was linear elastic. The Young's modulus of this model was taken as 70 GPa and the Poisson's ratio was taken as 0.3. Also in all the analyses the base nodes of the model container were held in both horizontal and vertical directions as indicated in Fig. 3.

#### ***Mohr Coulomb Model V***

The key aspect of applying FE to geotechnical problems is to take into account the plastic behavior of soil. Accordingly, many elasto-plastic models are used in the FE analysis. One of the simplest soil models is the Mohr-Coulomb type model. Such a model has been adapted to handle the elastic-perfectly plastic behavior of soil and is implemented into the FE code SWANDYNE [18]. The model is briefly outlined below and the actual parameters that are used are presented.

Since the primary concern is with granular material, the non-associated flow rule must be used. Many researchers have established that sandy soils follow the non-associative flow rule, for example, Desai and Siriwardane [21], Wood [22], Zhang et al [23], etc. The Mohr-Coulomb model in SWANDYNE was designed to give a non-associative Mohr-Coulomb elastic-perfectly plastic response. The features of this constitutive model include:

1. The variation of bulk and/or shear modulus with mean confining effective stress. The variation can be linear or square root.
2. Cohesion can be included. The stress state will be cut-off if the mean effective confining stress is more negative than the allowable cohesion.
3. The plastic potential can have a different slope with the yield surface.
4. A smooth fit to the triaxial compression and triaxial extension state so there is no corner or singularity in the  $\pi$ -plane [24].

The actual values used in all the analyses reported in this paper are presented in Table 2. It may be noted that the Mohr-Coulomb V model was chosen by setting the switch NCRIT=3. The square root variation in the soil moduli with confining stress was achieved by setting the switch NYOUNG=1. The soil was assumed to have a relative density of 40% to ensure liquefaction. The

dilatancy angle of the sand at this relative density was estimated using the dilatancy-relative density index relationship suggested by Bolton [25].

The Young's modulus for the soil was specified as 120 MPa at a mean effective confining stress of 100 kPa. This value was computed following the Hardin and Drenvich [26] equation for sandy soils,

$$G_{\max} = 100 \frac{(3-e)^2}{1+e} (p')^{0.5} \quad (1)$$

where  $G_{\max}$  is the small-strain shear modulus in MPa,  $e$  is the void ratio and  $p'$  is the mean confining stress in MPa. Knowing  $G_{\max}$  the Young's modulus can be calculated as

$$E = 2G_{\max} (1 + \nu) \quad (2)$$

Thus  $G_{\max}$  and hence  $E$  were calculated for  $p'=100$  kPa. The shear modulus and bulk modulus are specified to vary as a square root function with depth. It must be pointed out that as the FE analyses presented here are elasto-plastic, the value of Young's modulus specified in Table 1 is only used at the start of the analyses. In subsequent iterations, the value of all the moduli are updated according to the stress and strain increments.

### *P-Z Mark III model*

In order to capture the cyclic behaviour of saturated sand the P-Z Mark III model that was developed by Pastor et al [27] was used. This model was used by several researchers to study earthquake induced excess pore pressure generation in saturated sands, for example, Chan et al [28], Madabhushi and Zeng [19], Dewoolkar et al [29], Haigh et al [20]. The P-Z Mark III model is a generalized plasticity-bounding surface model that accommodates the non-associated flow rule. The model is described by means of potential surfaces that are given by the equation

$$G(p', q, p_g) = \left\{ q - M_g p' \left( 1 + \frac{1}{\alpha_g} \right) \left[ 1 - \left( \frac{p'}{p_g} \right)^{\alpha_g} \right] \right\} \quad (3)$$

where  $p'$  = mean confining stress;  $q$  = deviatoric shear stress;  $M_g$  = slope of the critical state line;  $\alpha_g$  = constant and  $p_g$  = size parameter. The same type of function described in Eq.3 above is assumed for the yield surface. The parameter  $M_g$  is obtained from the angle of friction  $\phi'$  of the soil and Lode's angle  $\theta$  by the Mohr-Coulomb relation as;

$$M_g = \frac{6 \sin \phi' \sin 3\theta}{3 - \sin \phi' \sin 3\theta} \quad (4)$$

To find the value of  $M_g$  at different values of  $\theta$ , the value of  $\sin \phi'$  is assumed to be constant. When  $\theta = \pi/6$ ,  $M_g$  is taken as  $M_{gc}$ , which is obtained from triaxial compression tests. The dilatancy of sand in the P-Z Mark III model is approximated using the linear function of the stress ratio  $\eta = q/p'$  as suggested by Nova and Wood [30] as

$$d = (1 + \alpha_g)(M_g - \eta) \quad (5)$$

The direction of the plastic flow is defined by means of a unit normal,  $n_g$ , given as

$$\{n_g\} = \left( \frac{1}{\sqrt{1 + d^2}} \right) \{d, s\}^T \quad \text{for loading,} \quad (6)$$

$$\{n_g\} = \left( \frac{1}{\sqrt{1 + d^2}} \right) \{abs(d), -s\}^T \quad \text{for unloading,} \quad (7)$$

where  $s = 1$  during compression; and  $s = -1$  during extension. The P-Z model includes the non-associated flow by separating the yield surface and the plastic potential surface. The yield or bounding surface  $F$  is assumed to have a form similar to that of the plastic potential surface  $G$ , but has different parameters  $M_f$ ,  $\alpha_f$ , and  $p_f$ , instead of  $M_g$ ,  $\alpha_g$ , and  $p_g$ . Therefore Eqs. 5 to 7 can be written for the yield surface using these parameters. In addition to this the plastic modulus for loading is obtained as

$$H_L = H_o p' \left( 1 - \frac{\eta}{\eta_f} \right)^4 [H_v + H_s] \quad (8)$$

where

$$\eta_f = \left(1 + \frac{1}{\alpha_f}\right) M_f \quad (9)$$

$$H_v = 1 - \frac{\eta}{M_g} \quad (10)$$

$$H_s = \beta_o \beta_1 e^{-\beta_o \varepsilon} \quad (11)$$

$$\varepsilon = \int |d\varepsilon_q^p| \quad (12)$$

where  $H_o$ ,  $\beta_o$ , and  $\beta_1$  are model parameters; and  $d\varepsilon_q^p$  = plastic deviatoric strain increment. The undrained triaxial tests predict rapid pore pressure build up on unloading. This highlights the necessity to predict plastic strains on unloading by the constitutive model. In P-Z Mark III model the following expression is used for unloading plastic modulus  $H_u$ ;

$$H_u = H_{uo} \left( \frac{\eta_u}{M_g} \right)^{-\gamma_u} \quad (13)$$

where  $\eta_u$  = stress ratio at which unloading takes place; and  $H_{uo}$  and  $\gamma_u$  are model parameters.

The model parameters for the P-Z Mark III model used during the analyses presented in this paper are presented in Table 3.

### ***Ground motions***

For the analyses described in this paper two types of ground motions were considered. Firstly a sinusoidal motion that had 10 cycles of shaking with a linear build-up over 4 cycles and linear decrease over 4 cycles was used. The peak magnitude of the acceleration was  $\pm 5 \text{ m/s}^2$  (or  $\sim 0.5g$ ) and the duration of the earthquake was 8 seconds. This input motion can be seen in Fig. 6.

Secondly, a more realistic earthquake motion from the Kobe earthquake of 1995 in Japan was used. This motion had a peak ground acceleration  $+6 \text{ m/s}^2$  (or  $\sim 0.6g$ ) and  $-8 \text{ m/s}^2$  (or  $\sim -0.8g$ ) and can be seen in Fig. 7. Although this earthquake had larger peak accelerations, these are reached in relatively few number of cycles that occur in the first few seconds of this earthquake motion. As explained earlier these motions were applied as acceleration inputs to all of the base nodes shown in Fig. 3.



## Static Analysis

In any numerical analysis it is important to verify that the static equilibrium has been established first before attempting the earthquake analysis. As explained earlier a static run was first carried out to establish the geo-static stresses in the soil elements in the presence of the buoyant tunnel (see Fig. 2). In Fig. 4 the contours of vertical effective stresses established during the static analysis are presented. In this figure it can be seen that the vertical effective stresses decrease below the tunnel as indicated by the lowering of the contours. This is to be anticipated as the tunnel is buoyant, it unloads the soil below the base of the tunnel leading to a drop in vertical effective stresses. The opposite is true above the tunnel. As the tunnel is trying to float up, there is an increase in the vertical effective stresses in this region as indicated by the higher value contours in this region in Fig. 4. The FE analyses is therefore able to capture the buoyant behaviour of the tunnel. It must be noted that the tunnel does not actually suffer any uplift during this phase as the factor of safety against floatation is quite high (a FoS of 1.6).

In Fig. 5 the contours of hydrostatic pore pressures established during the static run are presented. As expected, these contours are all horizontal confirming that equilibrium has been reached. Further the maximum hydrostatic pressure at the base of the problem is about 186.4 kPa, which is the correct water pressure at a depth of 19 m.

## Response of rectangular tunnel to earthquake loading

The response of the tunnel to the sinusoidal motion is considered first. In Fig. 6 the applied ground motion to the base nodes, the response of the tunnel in the form of the horizontal acceleration recorded on the tunnel and the acceleration of the soil surface node above the tunnel are presented as time histories. In this figure we can see that the response of the tunnel has attenuated significantly relative to the input motion. This is due to the liquefaction of the soil around the tunnel and the consequent isolation of the tunnel structure from the ground motions. The peak accelerations of the tunnel are only  $\pm 2 \text{ m/s}^2$ . Similarly the ground surface is also isolated due to the soil liquefaction. The peak ground accelerations are only  $\pm 1 \text{ m/s}^2$ .

The sinusoidal input motion considered has a large number of rather strong accelerations. To contrast with this, the ground motions recorded during Kobe earthquake as described earlier were also considered. In Fig. 7, the Kobe motion applied to the base nodes, the response of the tunnel and the ground surface are presented. In this figure it is again seen that both the tunnel and the ground surface are significantly isolated from the ground motion, again due to the soil liquefaction. The horizontal accelerations on the tunnel are  $+1.5 \text{ m/s}^2$  and  $-3 \text{ m/s}^2$  showing significant attenuation but also reflecting the asymmetry in the input Kobe motion. The soil surface accelerations are about  $\pm 1.5 \text{ m/s}^2$  again showing significant attenuation.

## Uplift of the rectangular tunnel

One of the important design considerations for the cut-and-cover tunnels is the uplift they may suffer following earthquake induced liquefaction. This is particularly true when the tunnel lengths are long, running through liquefiable and non-liquefiable soil strata. Even small uplift of some sections of tunnel following soil liquefaction can result in opening up of transverse joints causing flooding of the tunnel.

The uplift of the tunnel recorded during the sinusoidal earthquake is presented in Fig. 8 along with the input motion. In this figure the surface heave recorded above the centre line of the tunnel is also presented. The uplift suffered by the tunnel is about 210 mm which is quite significant. The soil heave recorded is slightly less at 180 mm. This suggests that compressive axial strains are developing in the soil above the tunnel as the tunnel suffers uplift.

The uplift of the tunnel recorded during the Kobe earthquake is presented in Fig. 9 along with the input motion and the surface heave. The same vertical scale was used for Figs. 8 and 9 to allow direct comparison. The uplift suffered by the tunnel in this case was only about 50 mm which is much smaller than the sinusoidal earthquake case. The soil heave recorded was also slightly less at 40 mm. This again suggests that compressive axial strains are developing in the soil above the tunnel, as the tunnel suffers uplift.

Both Figs 8. and 9 show that the uplift of the tunnel does not coincide with the beginning of the earthquake motion, but starts sometime after. This will be explained in the next section. Further comparison of Figs. 8 and 9 suggests that the smaller number of cycles in the Kobe motion has resulted in much smaller uplift compared to the sinusoidal motion. This may indicate the importance of considering a wide variety of ground motions when attempting design of the rectangular tunnels in liquefiable soils. Similar observations on settlement of shallow and deep foundations on liquefiable soils were made by Madabhushi and Haigh [31] who commented on the relationship between the settlement of these structures that occur during the active part of the earthquake i.e. loading cycles.

## Excess pore pressure generation around the tunnel

The generation of excess pore pressures in the soil governs the tendency of the soil to liquefy and hence the ensuing uplift of the tunnel. Fig. 10 presents the generation of excess pore pressures below and above the tunnel as the sinusoidal earthquake is applied. The applied cyclic shearing causes the loose soil to attempt to contract. However, the pore fluid cannot drain sufficiently quickly to allow the change in volume, and hence positive excess pore pressures are generated. These in turn imply a drop in effective stress in the soil, or equivalently a loss of shear strength. The excess pore pressures

become equal to the total stress values at approximately 2 seconds, at which time full liquefaction has occurred, and as Fig. 8 shows the tunnel begins to uplift. Similarly, Fig 11 gives the equivalent plots using the Kobe earthquake input motion and again the beginning of the tunnel uplift coincides with the near full liquefaction of the soil. The tunnel will actually begin to uplift prior to full liquefaction as the buoyancy forces can overcome some shear strength in the soil.

Comparing Figs. 8 and 10 show that as the tunnel uplifts the excess pore pressure below the tunnel reduces. During the rapid cyclic shearing caused by the sinusoidal earthquake the sand has insufficient time to undergo volumetric strains and instead generates excess pore pressures. Following full liquefaction, the soil dilates along the critical state line towards the new unique combination of stress state and voids ratio causing the so-called ‘dilation spikes’ manifested as small cycles in excess pore pressures seen in Fig.10. As the tunnel uplifts, the soil beneath the tunnel experiences negative excess pore pressures or suctions superposed onto the positive excess pore pressure. These suction forces counter the buoyancy forces causing the uplift of the tunnel, hence the approximately linear uplift-time motion as seen in Fig. 8. As the earthquake motion stops, the surrounding soil regains shear strength and both the excess pore pressure and tunnel uplift plateau. As the tunnel uplift ceases fully, there will be pore pressure redistribution with pore fluid migrating to regions below the tunnel. This effect is manifested as a slight increase in the excess pore pressure beyond 9 seconds in Fig. 10. The excess pore pressures above tunnel remain unaffected as seen in Fig. 10. They simply reach the full liquefaction values and apart from the dilation spikes remain constant throughout the earthquake and will eventually dissipate as the soil starts to reconsolidate.

During the earthquake, the spatial distribution of excess pore pressures can be used to verify the above observations. Fig. 12 plots the contours of excess pore pressure ratio  $r_u$  defined in equation 14, at time 5 seconds.

$$r_u = \frac{u_{excess}}{\sigma'_v} \quad (14)$$

The contours in Fig. 12 indicate the degree of liquefaction suffered by different regions of the soil while the earthquake is occurring. The results are in agreement with those implied by Fig. 8 and 10. The soil above the tunnel and in the far-field is fully liquefied (i.e.  $r_u \approx 1$ ) allowing the tunnel to uplift. Beneath the tunnel, the darker contours indicate the region of soil which is only partially liquefied due to the balance between the positive excess pore pressures from the cyclic shearing and the negative excess pore pressures or suctions due to the tunnel uplift. The degree of liquefaction increases outwardly from the centre of this partially liquefied region as the drainage distance to the fully liquefied soil decreases.

Fig. 12 also shows the deformation undergone by the soil mesh in the FE analysis, magnified by a factor of 3 for clarity. In this figure the soil heave above the tunnel is quite apparent relative to the general settlement of the free-field.

### Effect of soil permeability on tunnel uplift

The floatation of the tunnel following soil liquefaction is dependent upon the tendency of the soil to generate and retain excess pore pressures. The critical soil properties which determine the generation and dissipation of excess pore pressures are the relative density and the soil permeability  $k$ .

The effect of the relative density on excess pore pressure generation has been previously investigated by many researchers [31]. In this paper, the main focus is on tunnel uplift once full liquefaction has occurred. Therefore the effect of soil permeability which controls the dissipation of the excess pore pressures is investigated. Haigh et al [32] emphasise the importance of soil permeability in very low effective stress environment such as soil liquefaction. It must be pointed out that for the analyses described in this section, only the soil permeability values were changed without altering the soil strength or constitutive parameters. As a result, the peak excess pore pressures generated have not changed. However, the rate of dissipation changes, and hence the uplift mechanism of the tunnel is affected. In the analyses presented in this paper, the bottom boundary is assumed to be impervious. This would simulate the presence of intact bedrock below the soil layer. The distance of the base of the tunnel from this interface is taken as 5 m as seen in Fig. 2. This is considered sufficient distance to the hydraulic boundary, which was confirmed by the excess pore pressure contours considered later in the paper (see Fig. 12).

A series of 7 analyses were carried out with a range of permeabilities from  $1 \times 10^{-7}$  to 0.5 m/s. In Fig. 13 the absolute uplift of the tunnel is plotted for these 7 analyses. For fine soils, with permeabilities less than  $1 \times 10^{-2}$  m/s the tunnel suffers upward floatation resulting in absolute uplift. Further, increasing the permeability results in the tunnel suffering settlement, as seen in Fig. 13. While the upward floatation is expected, the settlement of the tunnel in very permeable soils is counterintuitive. This will be explained later by considering the axial strains.

In addition to the tunnel uplift, it is important to consider the amount of soil heave that occurs at the ground surface above the centreline of the tunnel. These are plotted for the 7 analyses described above in Fig. 14. Similar to Fig 13, the finer sands exhibit absolute soil heave due to the uplifting tunnel whereas the coarse sands again suffer settlements.

However, in the case of these coarser sands the magnitude of the ground settlement is larger than the tunnel settlement. It is hence instructive to consider the average axial strain in the soil between the tunnel and the ground surface. Fig. 15 presents the relation between the soil permeability and the

average axial strain in this region of the soil. It becomes clear that in all cases the soil experiences compressive axial strains due to the relative movement between the settling soil surface (from post-earthquake consolidation) and the uplifting tunnel (from buoyancy forces). The relationship seen in Fig. 15 is non-linear, and the rate of change of axial strains decrease with decreasing permeability i.e. the axial strains are not affected by the permeability beyond a certain value. For the problem geometry and soil properties used in these analyses, this value is approximately  $1 \times 10^{-4}$  m/s from Fig. 15.

From a design viewpoint, the main consideration may be the absolute movement of the tunnel. Both tunnel uplift and tunnel settlement can compromise the structural integrity of the tunnel with transverse joints between tunnel segments opening gaps. This can lead to uncontrolled flooding and, further, loss of important infrastructure in the critical post-earthquake period.

## Conclusions

In this paper, the floatation of a rectangular tunnel following earthquake-induced soil liquefaction was investigated using dynamic finite element analyses. Two types of earthquake input motions were considered; firstly the traditional sinusoidal motion of 10 cycles was used with a ramp-up and ramp-down cycles at the start and end of the earthquake and secondly the realistic earthquake motion recorded during the Kobe earthquake of 1995 in Japan. In each case the tunnel accelerations and surface accelerations were shown to attenuate significantly due to the onset of liquefaction. The uplift of tunnels following soil liquefaction is a major design consideration for cut-and-cover type rectangular tunnels often used for underground transportation links such as metro lines. The uplift of the tunnel following soil liquefaction and ground surface heave were investigated for both sinusoidal and Kobe motion. It was shown that the sinusoidal motion resulted in much larger uplift and heave compared to the Kobe motion. This highlights the importance of establishing the tunnel uplift under a variety of earthquake motions for design purposes. The generation of excess pore pressures in the soil were also investigated in regions adjacent to the tunnel. It was shown that for the sinusoidal motion, the soil above the tunnel reaches full liquefaction whilst the region of soil below the tunnel starts to generate excess pore pressures which are quickly overcome with relative suctions once the tunnel uplift begins. For the Kobe motion this effect was not present owing to relatively small uplift the tunnel suffered.

Finally the effect of soil permeability on tunnel uplift was investigated by conducting the dynamic FE analyses with 7 different soil permeabilities. It was shown that the tunnel suffers absolute uplift when soil permeability was low but this trend changes to absolute settlements when soil permeability is large. The ground surface heave and settlement also mirror this behaviour. When average axial strains are considered for the region of soil above tunnel, it is clear that for all cases of permeabilities

compressive axial strains are observed. These compressive axial strains decrease with decreasing permeability before reaching a plateau beyond which the permeability has no affect. The larger permeability soils are able to dissipate significant excess pore pressures and undergo consolidation settlements quickly and the tunnel uplift is ‘drowned’ out in these settlements. For finer soils with low permeability the dissipation of excess pore pressure is slow and therefore the tunnel suffers absolute uplift.

From a design point of view, both tunnel uplift and settlement can be detrimental as movement of individual segments of the tunnels can open gaps between transverse joints of the tunnel that can lead to flooding and a consequent loss of infrastructure.

## References

- [1] Cilingir, U. and Madabhushi, S.P.G., (2011a). A model study on the effects of input motion on the seismic behaviour of tunnels, *Journal of Soil Dynamics and Earthquake Engineering*, Vol. 31, pp. 452-462.
- [2] Cilingir, U. and Madabhushi, S.P.G. (2011b). Effect of depth on the seismic behaviour of circular tunnels. *Canadian Geotechnical Journal* 48, 117-127.
- [3] Cilingir, U. and Madabhushi, S.P.G., (2011c), Effect of depth on the seismic response of square tunnels, *Soils and Foundations*, Vol.51, No.3., Japanese Society of Soil Mechanics, Tokyo.
- [4] Tokimatsu, K., Tamura, S., Suzuki, H. and Katsumata, K. (2011). Quick Report on Geotechnical Problems in the 2011 Tōhoku Pacific Ocean Earthquake [In Japanese]. [Online] <<http://eqclearinghouse.cuee.titech.ac.jp/groups/Tōhoku2011/wiki/01411/Geohazard.html>>
- [5] Yang, D., Naesgaard, E., Byrne, P.M., Adalier, K. and Abdoun, T. (2004). Numerical model verification and calibration of George Massey Tunnel using centrifuge models. *Canadian Geotechnical Journal* 41, 921-942.
- [6] Sun, Y., Klein, S., Caulfield, J., Romero, V. and Wong, J. (2008). Seismic analyses of the Bay Tunnel. *Proceedings of the International Conference on Geotechnical Earthquake Engineering and Soil Dynamics IV*, Sacramento.

- [7] Adalier, K., Abdoun, T., Dobry, R., Phillips, R., Yang, D. and Naesgaard, E. (2003). Centrifuge modeling for seismic retrofit design of an immersed tube tunnel. *Journal of Physical Modelling of Geotechnics* 3, No. 2, 23-32.
- [8] Chou, J.C., Kutter, B.L., Travarasrou, T. and Chacko, J.M. (2011). Centrifuge modeling of seismically induced uplift for the BART Transbay Tube. *Journal of Geotechnical and Geoenvironmental Engineering* 137, No. 8, 754-765.
- [9] Sasaki, T., Matsuo, O. and Kondo, K. (1999). Centrifuge model tests on uplift behavior of buried structures during earthquakes, *Earthquake Geotechnical Engineering*, 315-320.
- [10] Tobita, T., Kang, G-C. and Iai, S., (2012), Estimation of Liquefaction-Induced Manhole Uplift Displacements and Trench-Backfill Settlements. *Journal of Geotechnical and Geoenvironmental Engineering*, Vol. 138, No. 4, April 2012, pp. 491-499
- [11] Ling, H.I., Mohri, Y., Kawabata, T., Liu, H., Burke, C. and Sun, L., (2003), Centrifugal Modeling of Seismic Behavior of Large-Diameter Pipe in Liquefiable Soil, *J. Geotech. Geoenviron. Eng.*, 129(12), 1092–1101.
- [12] Koseki, J. Matsuo, O. and Koga, Y. (1997). Uplift behavior of underground structures caused by liquefaction of surrounding soil during earthquake. *Soils and Foundations*, 37, 97-108.
- [13] Chian, S.C. and Madabhushi, S.P.G. (2012a). Excess pore pressures around underground structures in liquefiable soils. *Journal of Geotechnical Earthquake Engineering* 3, No. 2, 25-41.
- [14] Chian, S.C. and Madabhushi, S.P.G., (2012b), Effect of Buried Depth and Diameter on Uplift of Underground Structures in Liquefied Soils, *Journal of Soil Dynamics and Earthquake Engineering*, Volume 41, October 2012, pp. 181-190.
- [15] Chian, S., Tokimatsu, K., and Madabhushi, S. (2014). Soil Liquefaction–Induced Uplift of Underground Structures: Physical and Numerical Modeling. *J. Geotech. Geoenviron. Eng.* , 10.1061/(ASCE)GT.1943-5606.0001159.
- [16] Ling, H.I., Sun, L., Liu, H., Mohri, Y. and Kawabata, T., (2008), Finite element analysis of pipe buried in saturated soil deposit subjected to earthquake loading, *Journal of earthquake and Tsunami*, Vol. 2(1), DOI: 10.1142/S1793431108000244.

- [17] Chian, S.C. and Tokimatsu, K. (2012). Floatation of underground structures during the  $M_w$  9.0 Tōhoku Earthquake of 11th March 2011. Proceedings of the 15th World Conference on Earthquake Engineering, Lisbon, Paper ID 3705.
- [18] Chan, A.H.C., (1988), A generalised fully coupled effective stress based computer procedure for problems in Geomechanics, SWANDYNE User Manual, Swansea, UK.
- [19] Madabhushi, S.P.G. and Zeng, X. (1998). Seismic response of gravity quay walls. II: numerical modeling. *Journal of Geotechnical and Geoenvironmental Engineering*, ASCE, 124 (5), 418-427.
- [20] Haigh, S.K., Ghosh, B. and Madabhushi, S.P.G. (2003), A numerical investigation into effects of single and multiple frequency earthquake input motions, *Journal of Soil Dynamics and Earthquake Engineering*, Vol.23(8), pp 691-704.
- [21] Desai, C. S., and Siriwardane, H. J., 1984, *Constitutive Laws for Engineering Materials: With Emphasis on Geologic Materials*, Prentice Hall, Inc., Englewood Cliffs, New Jersey.
- [22] Wood, D.M., (2001), *Geotechnical Modelling*, Taylor and Francis, London.
- [23] Zhang, J., Stewart, D.P. and Randolph, M.F., (2002), Modeling of Shallowly Embedded Offshore Pipelines in Calcareous Sand, *J. Geotech. and Geoenviron. Engrg.*, Volume 128, Issue 5, pp. 363-371.
- [24] Zienkiewicz, O.C. and Pande, G.N., (1982), *Soil Mechanics, Transient & Cyclic Loads Constitutive Relations & Numerical Treatment*, Wiley.
- [25] Bolton M.D. (1986). The strength and dilatancy of sands. *Geotechnique* 36, No.1, pp 65-78.
- [26] Hardin, B. O. & Drnevich, V. P. (1972). Shear modulus and damping in soils: design equation and curves. *J. Soil Mech. Found. Engng. Div.*, ASCE 98, No. 7, 667–691.
- [27] Pastor, M., Zienkiewicz, O.C. and Leung, K.H., (1985). Simple model for transient soil loading in earthquake analysis. II: Non-associative models for sands, *Int. Journal of Numerical and Analytical Methods in Geomechanics*, Vol.9, pp 477-498.
- [28] Chan, A.H.C., Famiyesin, B.O., Madabhushi, S.P.G., and Wood, D.M., (1994), Dynamic analyses of saturated soils: Comparison of implicit u-p and explicit u-w formulations and the effect of initial conditions, *Proc. XIII Intl. Conf. on Soil Mechanics and Foundation Engineering*, Vol.4., New Delhi, India.



- [29] Dewoolkar, M.M., Ko, H.Y., and Pak, R.Y.S. (2001). Seismic behavior of cantilever retaining walls with liquefiable backfills. *Journal of Geotechnical and Geoenvironmental Engineering*, ASCE, 127 (5), 424-435.
- [30] Nova, R. and Wood, D.M. (1982). A constitutive model for soil under monotonic and cyclic loading. *Soil mechanics-transient and cyclic loads*, G.N. Pande and O.C. Zienkiewicz, eds., John Wiley & Sons, Inc., New York, N.Y.
- [31] Madabhushi, S.P.G. and Haigh, S.K., (2012), How well do we understand earthquake induced liquefaction? *Indian Geotechnical Journal*, Vol. 42, Issue 3, pp. 150-160, DOI: 10.1007/s40098-012-0018-2.
- [32] Haigh, S.K., Eadington, J. and Madabhushi, S.P.G. (2012). Permeability and stiffness of sands at very low effective stresses, *Géotechnique* 62, No. 1, 69-75.



Figure 1

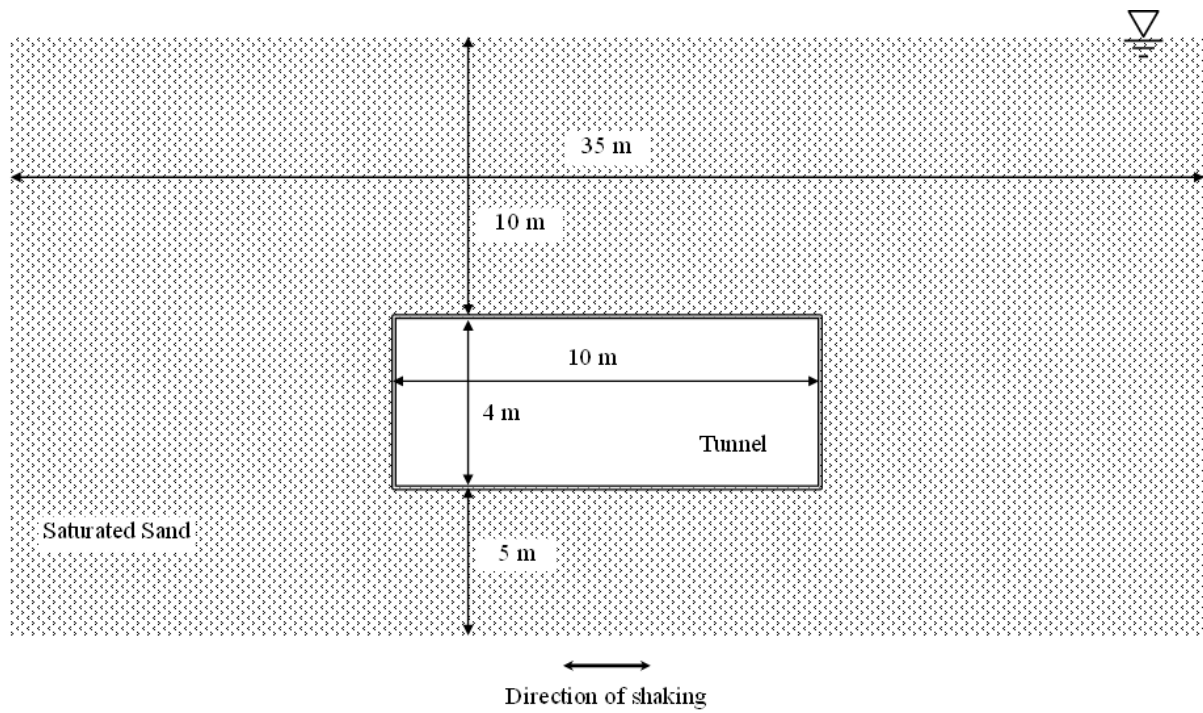


Figure 2

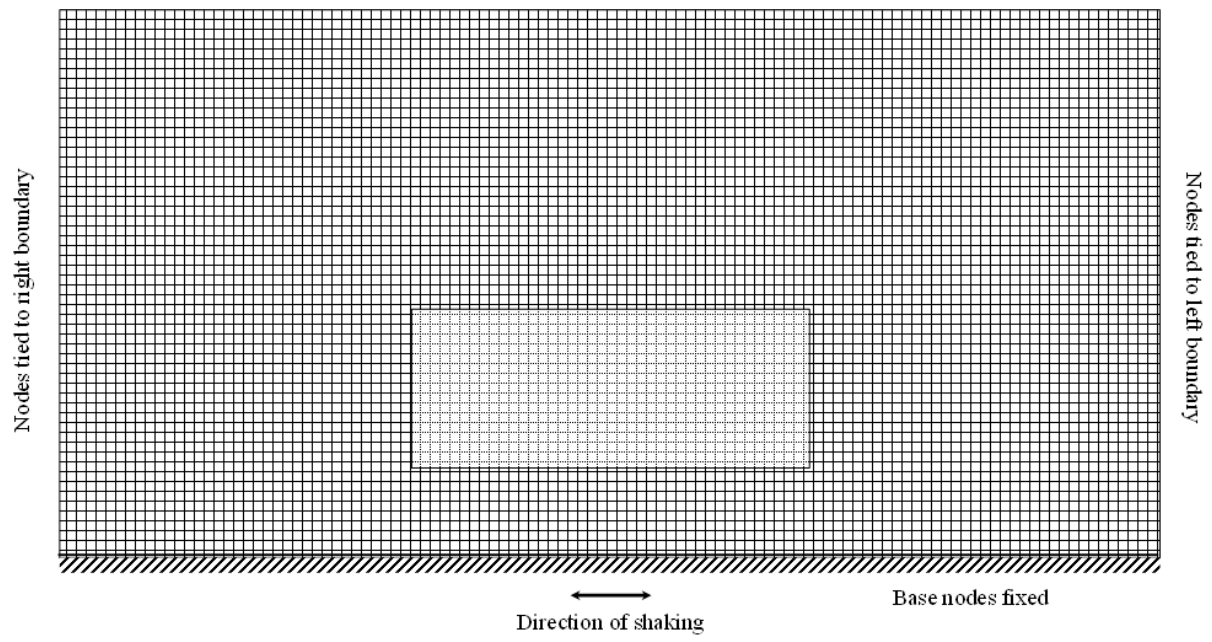


Figure 3

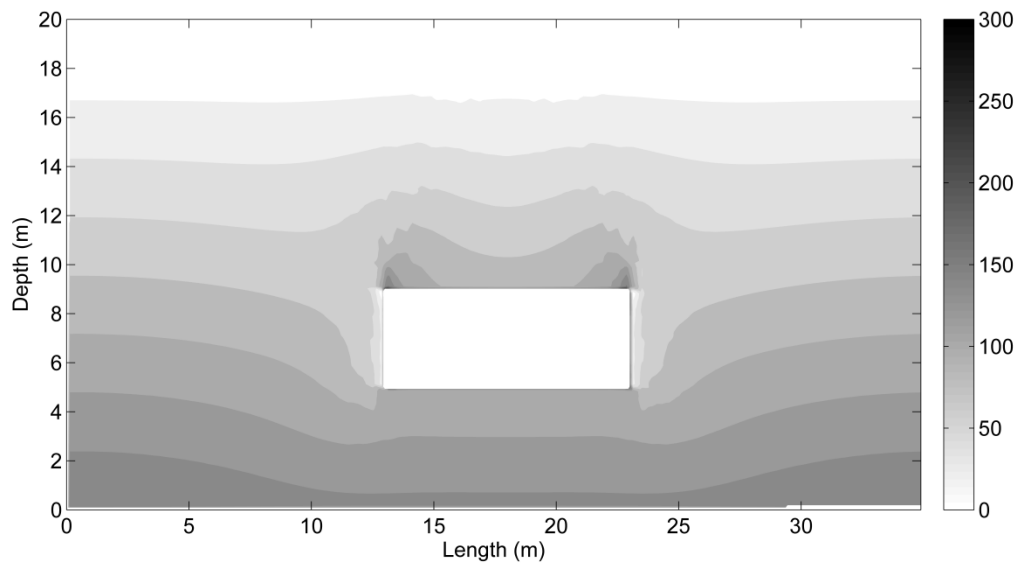


Figure 4

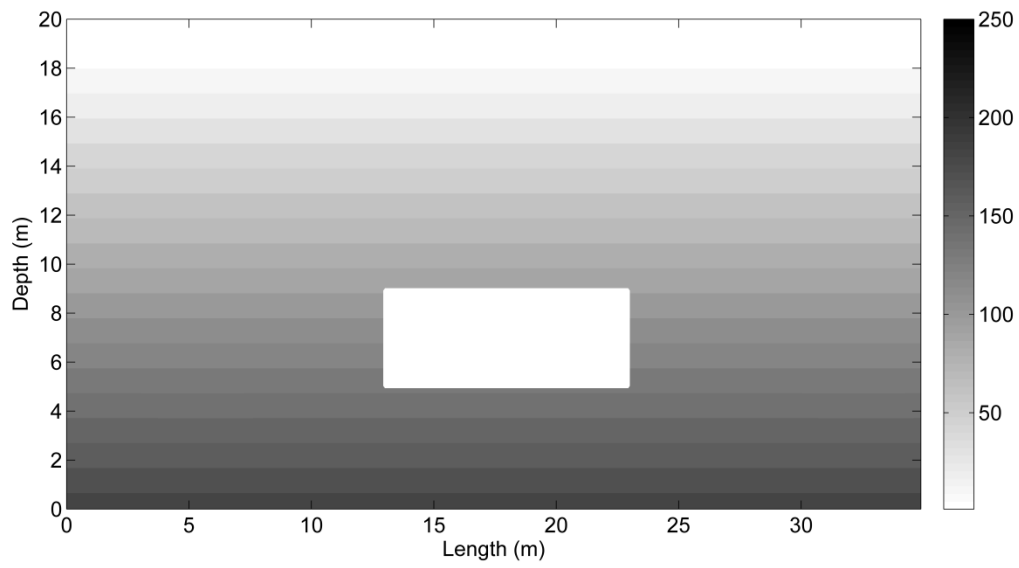


Figure 5

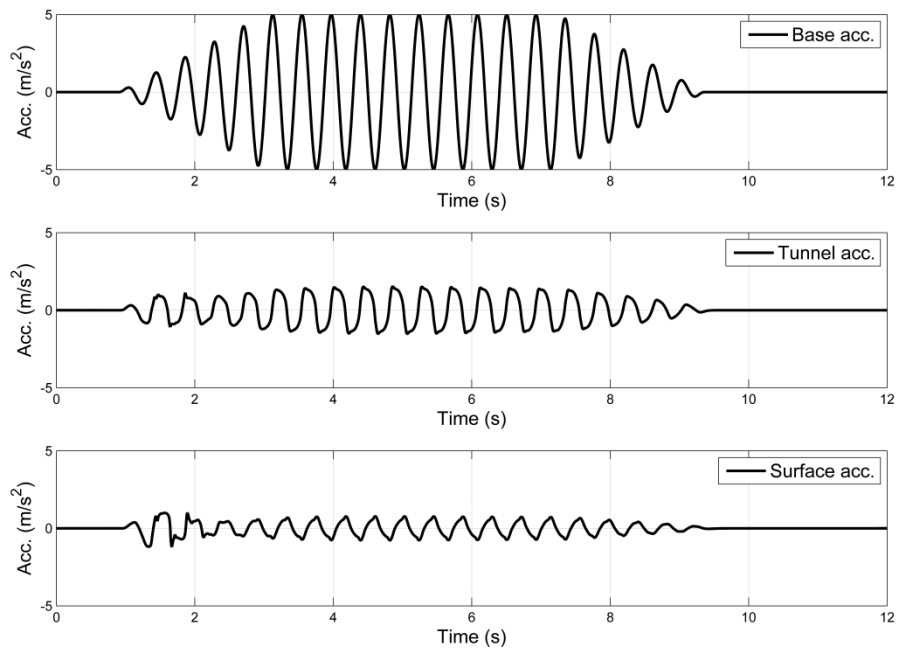


Figure 6

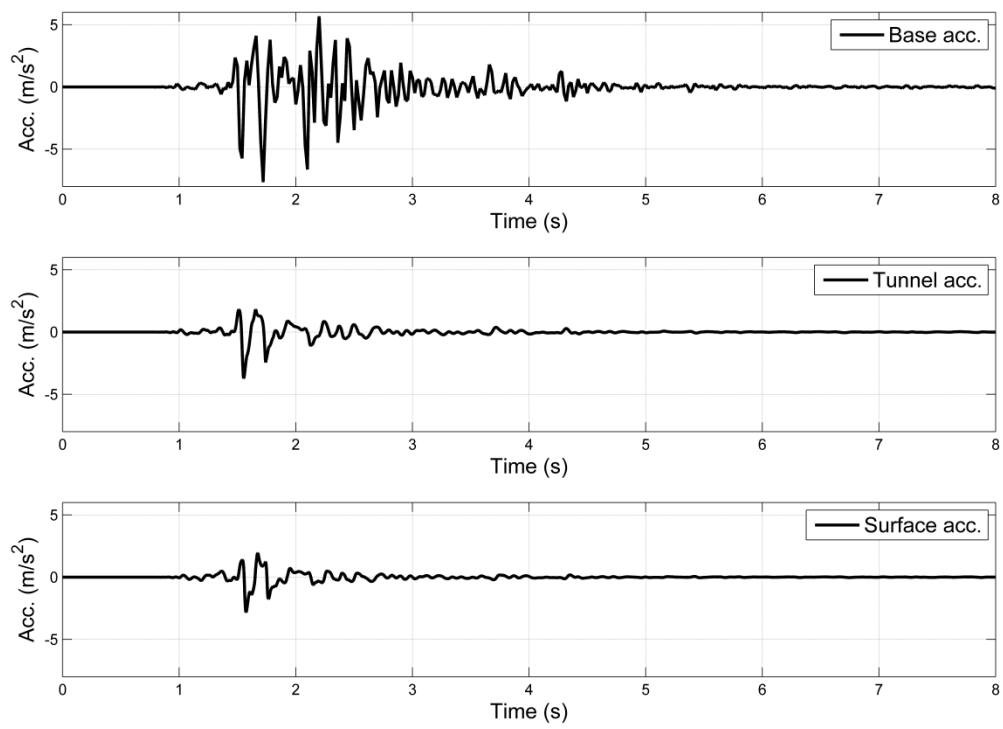


Figure 7

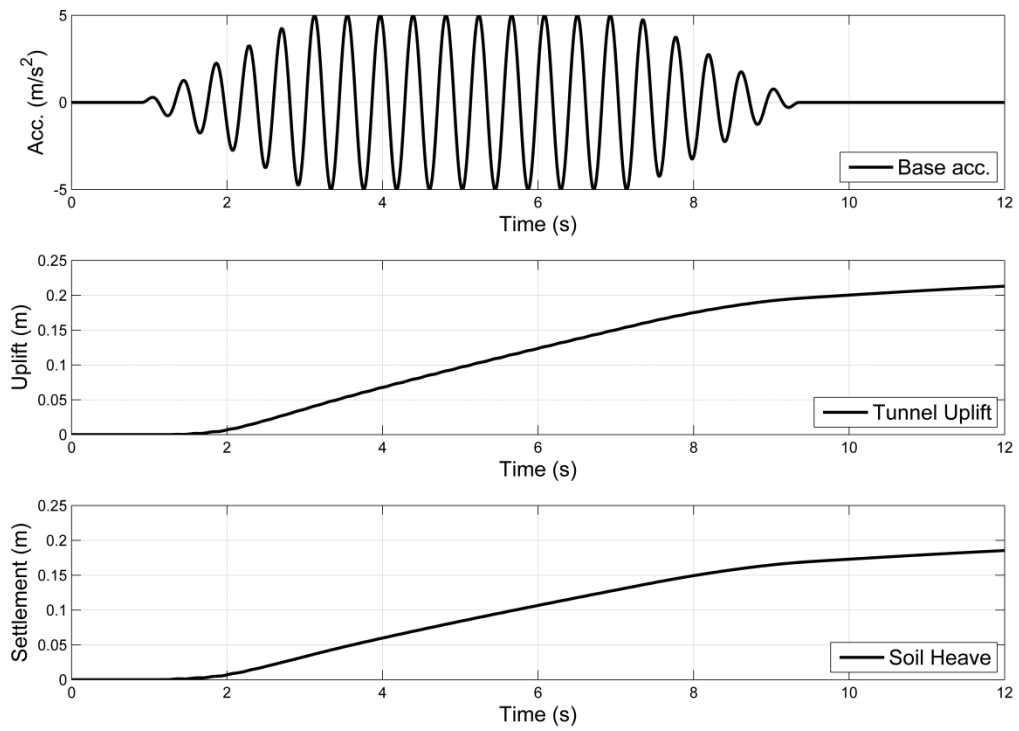


Figure 8

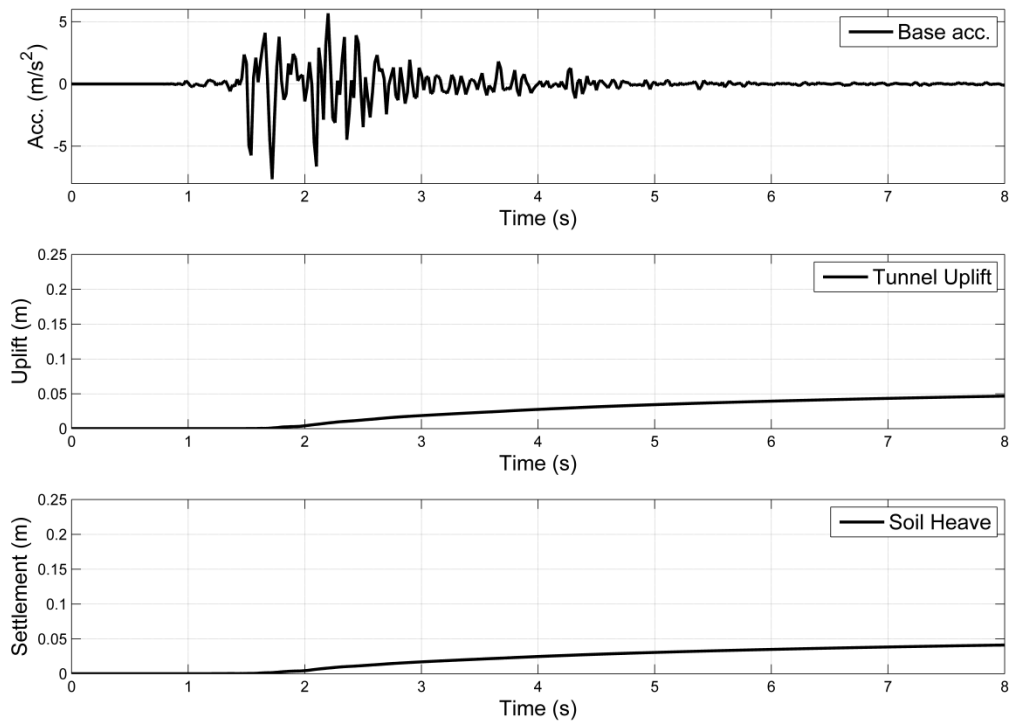


Figure 9

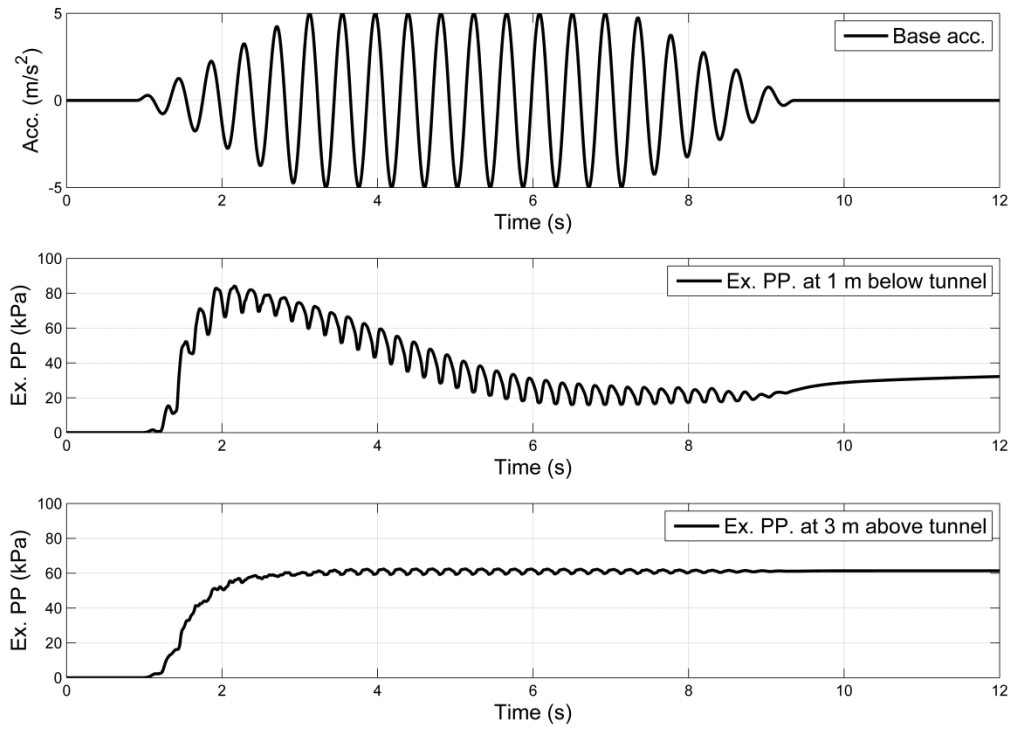


Figure 10

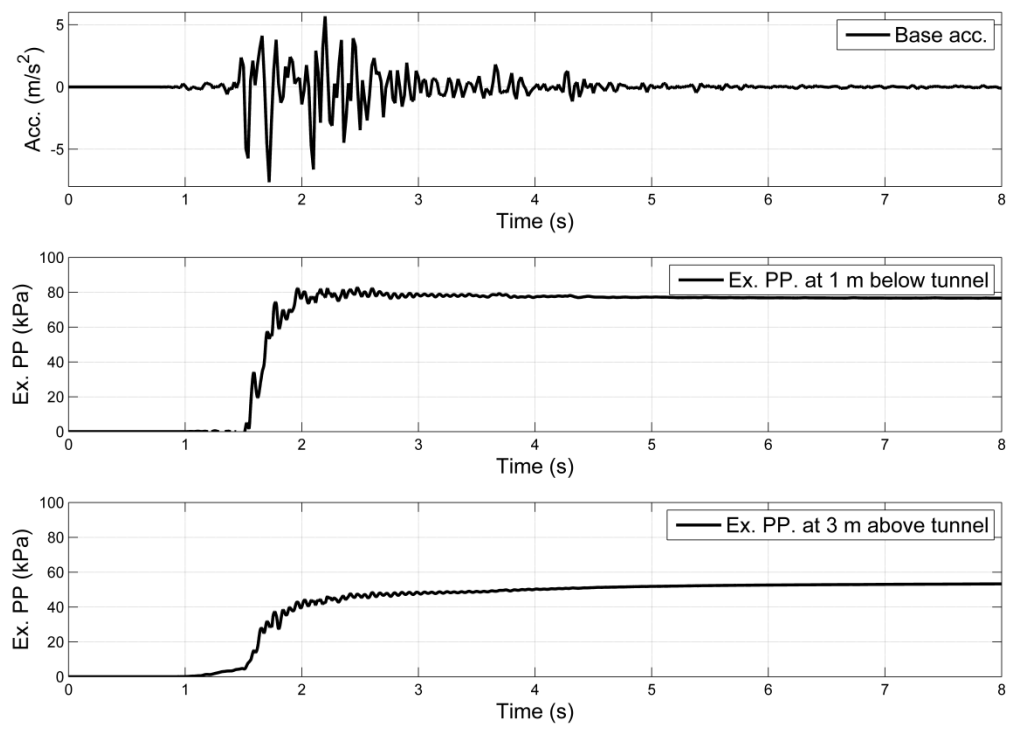


Figure 11

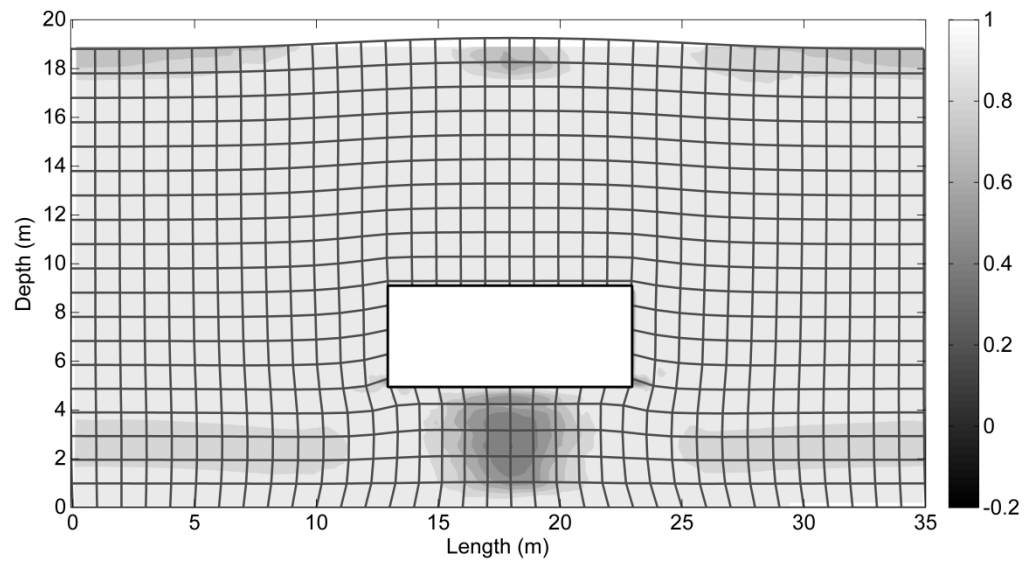


Figure 12

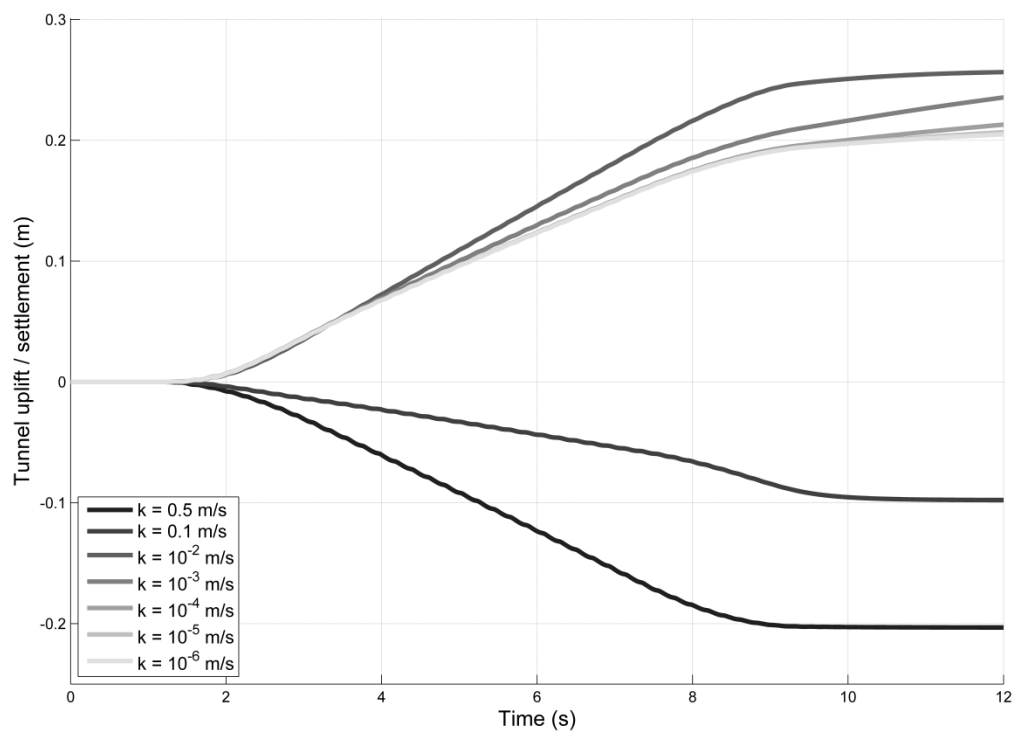


Figure 13

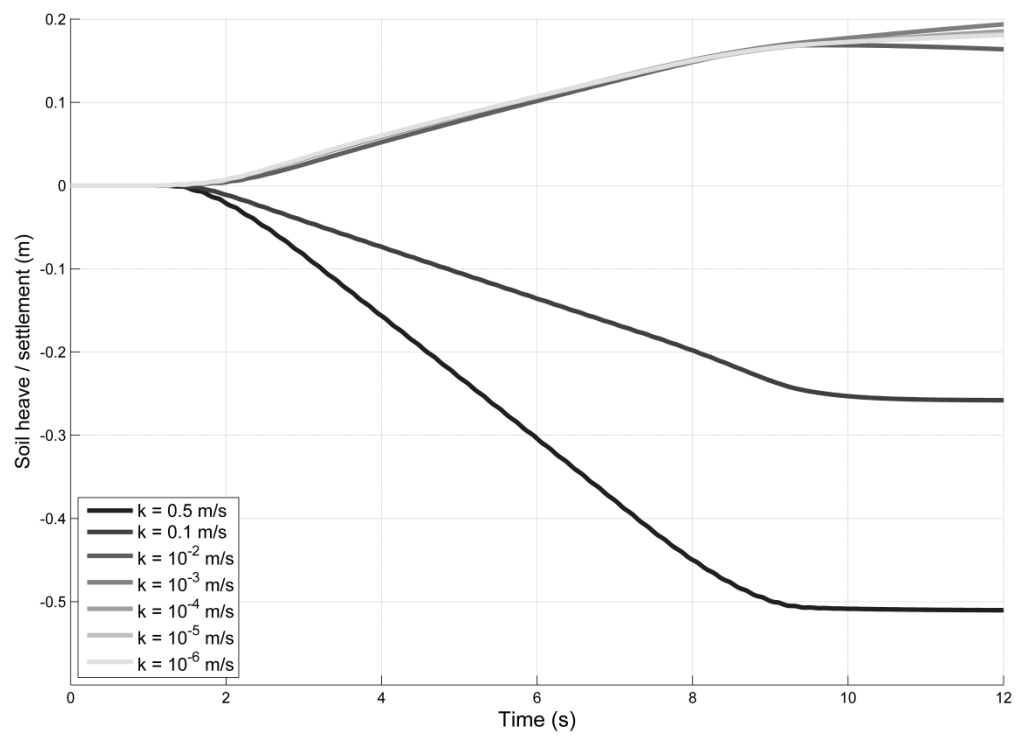


Figure 14



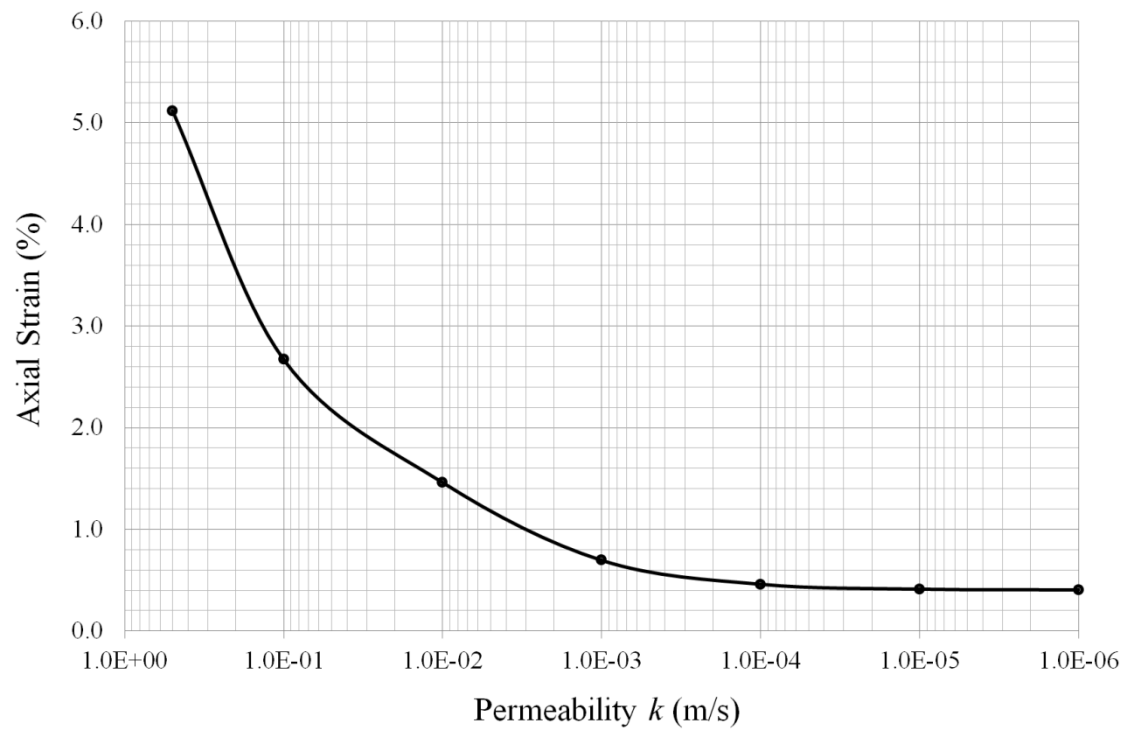


Figure 15

### **Figure captions**

Figure 1: A view of surface damage following floatation of a pipe line following the Tohoku earthquake of 2012 in Japan (Photo courtesy: Dr SC Chian, National University of Singapore)

Figure 2: Schematic diagram of the cross-section of the tunnel embedded in saturated sand layer

Figure 3: Schematic diagram showing the FE mesh discretisation and the boundary conditions

Figure 4: Contours of vertical effective stress (in kPa) following geo-static analysis

Figure 5: Contours of hydrostatic pore pressures (in kPa) following geo-static analysis

Figure 6: Acceleration time histories for sinusoidal earthquake motion

Figure 7: Acceleration time histories for Kobe earthquake motion

Figure 8: Uplift of tunnel and soil heave for sinusoidal earthquake motion

Figure 9: Uplift of tunnel and soil heave for Kobe earthquake motion

Figure 10: Excess pore pressures below and above tunnel for sinusoidal motion

Figure 11: Excess pore pressure below and above tunnel for Kobe motion

Figure 12: Contours of excess pore pressure ratio at 5 seconds into sinusoidal motion with an overlay of deformed mesh (magnification factor of 3)

Figure 13: Tunnel uplift / settlement for varying soil permeabilities

Figure 14: Soil heave / settlement at the surface for varying soil permeabilities

Figure 15: Variation of average axial strain with decreasing soil permeability

Table 1 Soil properties for numerical analyses

Parameter	Value
Soil saturated density (kN/m <sup>3</sup> )	18.91
void ratio	0.85
Friction angle	33°
Dilatancy angle	2°
Cohesion (kPa)	0
Permeability (m/s)	$1 \times 10^{-4}$
Initial Young's modulus of soil (MPa)	120
Initial bulk modulus of soil (MPa)	40

Table 2 Parameters for Mohr-Coulomb Five model

Parameter	Symbol	Saturated Case (Static analyses)
Young's Modulus for tunnel	E	70 GPa
Poisson's Ratio	$\nu$	0.3
Uniaxial yield stress or cohesion	$c'$	0 kPa
Work hardening modulus	H	100
Switch to select yield criterion	<b>NCRIT</b> NCRIT=1 $\Rightarrow$ Tresca NCRIT=2 $\Rightarrow$ Von Mises NCRIT=3 $\Rightarrow$ Mohr-Coulomb NCRIT=4 $\Rightarrow$ Drucker-Prager	<b>NCRIT</b> NCRIT=3 $\Rightarrow$ Mohr-Coulomb
Switch to select variation of soil moduli with depth	<b>NYOUNG</b> NYOUNG=0 $\Rightarrow$ no variation NYOUNG=1 $\Rightarrow$ specified by $\alpha$ NYOUNG=2 $\Rightarrow$ linear NYOUNG=3 $\Rightarrow$ square root	<b>NYOUNG</b> NYOUNG=1 $\Rightarrow$ specified by $\alpha$
Stress level at which moduli are prescribed	<b>PINIT</b>	100 kPa
Power of moduli change	$\alpha$	0.5

Table 3 Parameters for P-Z Mark III model used in the dynamic analyses

<b>Description of the parameter</b>	<b>Symbol</b>	<b>Value</b>
Slope of the critical state line (CSL) for plastic strain vector	$M_g$	1.15
Slope of the CSL for loading vector	$M_f$	0.75
Parameter to determine dilatancy using stress ratio	$\alpha_g$	0.4
Parameter to determine the dilatancy for the plastic strain vector	$\alpha_f$	0.02
Plastic modulus on loading	$H_{\text{loading}}$	200
Plastic modulus on unloading	$H_{\text{unloading}}$	$4 \times 10^8$
Parameter for plastic deformation during unloading	$\gamma_{Hu}$	2
Parameter for plastic deformation during reloading	$\gamma_{DM}$	0
Shear hardening parameter 1	$\beta_o$	4.2
Shear hardening parameter 2	$\beta_1$	0.2
Size parameter 1	$p_f$	0.5
Size parameter 2	$p_g$	0.5

